# The Metallicity of the Monoceros Stream

The Astrophysical Journal, 753:116 (12pp), 2012 July 10 doi:10.1088/0004-637X/753/2/116


# THE METALLICITY OF THE MONOCEROS STREAM*

Aaron M. Meisner[1,2], Anna Frebel[2,3], Mario Jurić[2,4], and Douglas P. Finkbeiner[1,2]
[1] Department of Physics, Harvard University, 17 Oxford Street, Cambridge, MA 02138, USA; ameisner@fas.harvard.edu
[2] Harvard-Smithsonian Center for Astrophysics, 60 Garden Street, Cambridge, MA 02138, USA; mjuric@cfa.harvard.edu, dfinkbeiner@cfa.harvard.edu
*Received 2011 December 19; accepted 2012 May 2; published 2012 June 20*

## ABSTRACT

We present low-resolution MMT Hectospec spectroscopy of 594 candidate Monoceros stream member stars. Based on strong color–magnitude diagram overdensities, we targeted three fields within the stream's footprint, with $178^\circ \leqslant l \leqslant 203^\circ$ and $-25^\circ \leqslant b \leqslant 25^\circ$. By comparing the measured iron abundances with those expected from smooth Galactic components alone, we measure, for the first time, the spectroscopic metallicity distribution function for Monoceros. We find the stream to be chemically distinct from both the thick disk and halo, with [Fe/H] $= -1$, and do not detect a trend in the stream's metallicity with Galactic longitude. Passing from $b = +25^\circ$ to $b = -25^\circ$, the median Monoceros metallicity trends upward by 0.1 dex, though uncertainties in modeling sample contamination by the disk and halo make this a marginal detection. In each field, we find Monoceros to have an intrinsic [Fe/H] dispersion of 0.10–0.22 dex. From the Ca II K line, we measure [Ca/Fe] for a subsample of metal-poor program stars with $-1.1 <$ [Fe/H] $< -0.5$. In two of three fields, we find calcium deficiencies qualitatively similar to previously reported [Ti/Fe] underabundances in Monoceros and the Sagittarius tidal stream. Further, using 90 spectra of thick disk stars in the Monoceros pointings with $b \approx \pm 25^\circ$, we detect a 0.22 dex north/south metallicity asymmetry coincident with known stellar density asymmetry at $R_{GC} \approx 12$ kpc and $|Z| \approx 1.7$ kpc. Our median Monoceros [Fe/H] $= -1.0$ and its relatively low dispersion naturally fit the expectation for an appropriately luminous $M_V \sim -13$ dwarf galaxy progenitor.

*Key words:* galaxies: dwarf – galaxies: interactions – Galaxy: evolution – Galaxy: stellar content – Galaxy: structure – stars: abundances

*Online-only material:* color figures

## 1. INTRODUCTION

The Monoceros stream (Newberg et al. 2002; Yanny et al. 2003, hereafter Y03) comprises a ring-like stellar overdensity in the plane of the Galactic disk. Between $110^\circ \lesssim l \lesssim 250^\circ$, the kinematically cold (Y03) stream covers $-30^\circ \lesssim b \lesssim 30^\circ$ at galactocentric radius $R \sim 17$–$19$ kpc with radial thickness $\Delta R \sim 4$ kpc (Jurić et al. 2008).

The true nature of the structure is still uncertain, with the leading scenarios being: (1) remnant of an accretion event (Peñarrubia et al. 2005), with the Canis Major dwarf galaxy (Martin et al. 2004) as a possible progenitor; (2) disturbance due to a high-eccentricity flyby encounter (Younger et al. 2008); and (3) disk flare or warp (e.g., Momany et al. 2006)

Discerning between these scenarios, especially the first two, may have important theoretical consequences as mergers with orbits and mass ratios implied by Peñarrubia et al. (2005) are deemed unlikely in current ΛCDM models (e.g., Younger et al. 2008).

In characterizing any stellar population, metallicity is considered a fundamental parameter. Unfortunately, the literature regarding the chemical composition of the Monoceros stream is sparse and seemingly inconsistent. For example, Y03 estimate [Fe/H] $\sim -1.6$ at $l = 198^\circ$, $b = 27^\circ$ using the Ca II K line and colors of turnoff stars. On the other end, Crane et al. (2003, hereafter C03) measure a mean of $-0.4 \pm 0.3$ using M-giants, sampled mainly from observations of the northern component of the stream. Most recently, using photometric metallicities, Ivezić et al. (2008, hereafter I08) find the MSTO stars in the northern anticenter portion of the stream to have a median metallicity of [Fe/H] $= -0.95$, with intrinsic rms scatter of only 0.15 dex. Hypotheses invoked to reconcile these values range from multiple stellar populations (e.g., Peñarrubia et al. 2005), to systematic errors in calibrations (C03), and to questioning whether the northern and southern part of the ring share the same origin (Conn et al. 2007). Also, except for the I08 photometric study, the full metallicity distribution function (MDF) of stars in the Monoceros stream has actually never been measured from spectroscopy.

To better characterize the chemical composition of Monoceros, we have obtained spectra of ∼600 candidate member stars. This large sample size allows us to probe the Monoceros MDF with good statistics. Also, by pointing in multiple directions along the stream, we can search for metallicity gradients. Specifically, we set out to characterize the [Fe/H] MDF of Monoceros in each of three fields with $177.^\circ9 \leqslant l \leqslant 202.^\circ9$ and $-24.^\circ2 \leqslant b \leqslant 24.^\circ4$ (see Table 1 for field details and naming conventions). Additionally, we aim to gauge the $\alpha$-enhancement of Monoceros from a [Ca/Fe] measurement. This allows us to address the origin of Monoceros by comparing its [Ca/Fe] to the differing $\alpha$-abundance patterns found in the Milky Way versus dwarf spheroidal (dSph) galaxies.

## 2. MMT OBSERVATIONS

### 2.1. Sample Selection

Recognized as a stellar overdensity between $b = \pm 30^\circ$ for $110^\circ \lesssim l \lesssim 250^\circ$, Monoceros appears most strikingly in the

* Observations reported here were obtained at the MMT Observatory, a joint facility of the Smithsonian Institution and the University of Arizona.
[3] Current address: Massachusetts Institute of Technology, Kavli Institute for Astrophysics and Space Research, 77 Massachusetts Avenue, Cambridge, MA 02139, USA; afrebel@mit.edu
[4] Hubble Fellow.

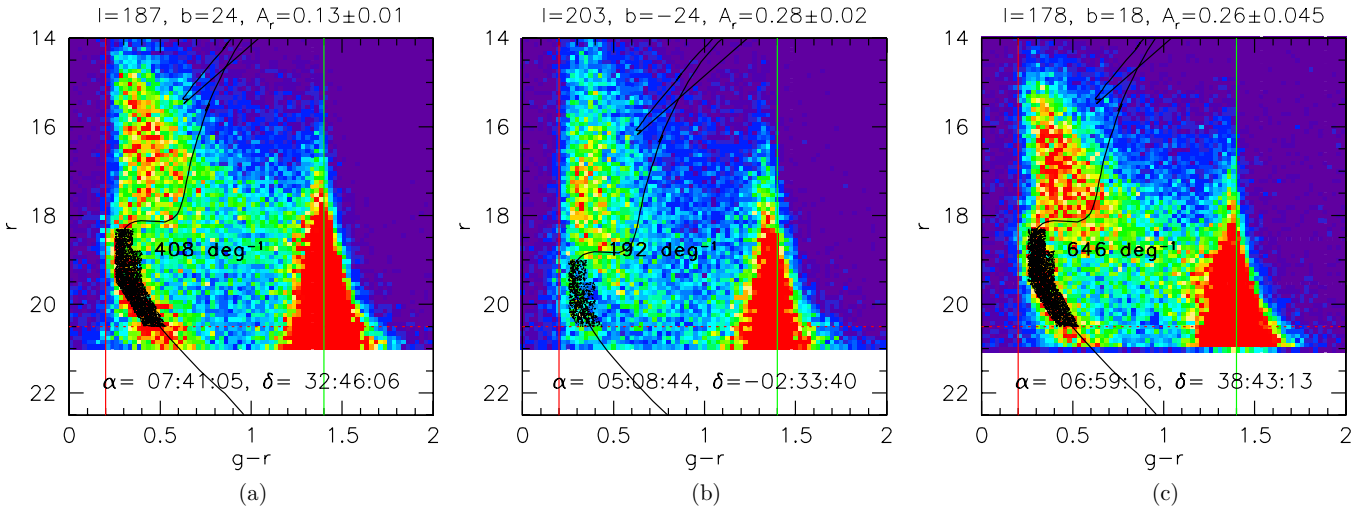


**Figure 1.** SDSS DR7 CMDs of target fields NORTH (a), SOUTH (b), and NORTH18 (c). All three panels have the same dynamic range (0–30 stars pixel$^{-1}$, with the pixel sizes being 0.025 mag and 0.1 mag in $g - r$ and $r$, respectively). The black dots represent Monoceros candidates from which the spectroscopic sample we analyzed was drawn. The black line shows an 8 Gyr, $Z = 0.0039$ isochrone (Marigo et al. 2008) intended only to guide the eye along the Monoceros MSTO.

(A color version of this figure is available in the online journal.)

**Table 1**
Summary of MMT Observations/Targets

| Sample | $l$ | $b$ | $\alpha$ | $\delta$ | Exposures (s) | $N_{\rm stars}$ | $(S/N)_{\rm med}$ | $r_{\rm med}$ | $\lvert Z\rvert_{\rm med}$[a] (kpc) | $A_r$ |
|---|---|---|---|---|---|---|---|---|---|---|
| | | | | NORTH | | | | | | |
| Monoceros | 187.°245 | 24.°401 | 115.°741 | 32.°662 | 2 × 7200 | 199 | 49 | 19.55 | 3.871 | 0.12 |
| Thick Disk | 187.°245 | 24.°401 | 115.°741 | 32.°662 | 2 × 7200 | 30 | 123 | 17.62 | 1.603 | 0.12 |
| | | | | SOUTH | | | | | | |
| Monoceros | 202.°884 | −24.°183 | 76.°908 | −2.°587 | 2 × 7200 | 146 | 47 | 19.83 | 4.911 | 0.30 |
| Thick Disk | 202.°884 | −24.°183 | 76.°908 | −2.°587 | 2 × 7200 | 60 | 137 | 17.44 | 1.788 | 0.30 |
| | | | | NORTH18 | | | | | | |
| Monoceros | 177.°879 | 18.°055 | 104.°834 | 38.°852 | 2 × 7200,5400 | 249 | 84 | 19.08 | 2.688 | 0.29 |
| | | | | M13 | | | | | | |
| Calibration | 58.°999 | 40.°917 | 250.°416 | 36.°454 | 3600 | 189 | 39 | 18.34 | 5.028 | 0.05 |

**Note.** [a] Using the photometric parallax relation of I08 equations (A6) and (A7).

number counts of MSTO F/G dwarfs at galactocentric distances $R \sim 15$–$20$ kpc. Near the Galactic anticenter, these stars correspond to apparent magnitude $r \approx 18.5$–$20.5$ and color $g - r \approx 0.25$–$0.4$, with $ugriz$ referring to Sloan Digital Sky Survey (SDSS) photometric passbands. By examining ($g$, $g - r$) color–magnitude diagrams (CMDs) of objects classified by the SDSS (DR7) as stars within the joint Monoceros/SDSS footprint, we identified many degree-scale pointings in which the Monoceros MSTO was obviously visible above the Galactic background (for background estimation details see Section 3.6). In the best cases, the relevant CMD region of such pointings exhibited a factor of ∼2 overdensity, with total projected density ∼200–300 stars deg$^{-2}$. This field size and target density matches that of MMT/Hectospec, which, with its large 6.5 m mirror size, can obtain at $r = 20$ S/N sufficient to measure [Fe/H] with integration times of ∼4 hr.

Hoping to gauge both $l$ and north/south gradients in the stream's metallicity, six such fields were initially targeted for MMT/Hectospec spectroscopy, covering $150° \lesssim l \lesssim 230°$ in the Galactic north and sampling four Galactic latitudes with $-30° < b < 30°$. In several of these fields, a relatively small subsample of much brighter thick disk targets were chosen from a similar range of MSTO $g - r$ colors and with $17 < r < 18$.

### 2.2. Observations and Data Reduction

The observations were carried out in MMT queue-scheduled multi-object observing mode. Due to a combination of factors, including weather, only three fields were observed, spanning a limited range of ($l$, $b$), though still including both Galactic north and south. Table 1 summarizes the targets/observations, and Figure 1 shows the CMD of each field, indicating targeted regions.

Hectospec can observe up to 300 objects at once. In general, we typically devoted ∼50 fibers to measuring the sky, with the remainder targeting Monoceros candidates subject to the constraints of the instrument (e.g., the availability of the targets in the desired magnitude range, and limits on how closely spaced the fibers could get). Any remaining fibers were set to target the thick disk stars to investigate the thick disk asymmetry present toward the Galactic anti-center (see Section 5.2). We used the 270 gpm grating yielding a resolving power of $R \sim 1000$ near 5000 Å. The low-resolution warrants full wavelength coverage of 3700–9150 Å.

The data were reduced with customized IRAF procedures as part of the SAO Telescope Data Center service (Mink et al. 2007). The signal-to-noise ratio (S/N) of the final spectra

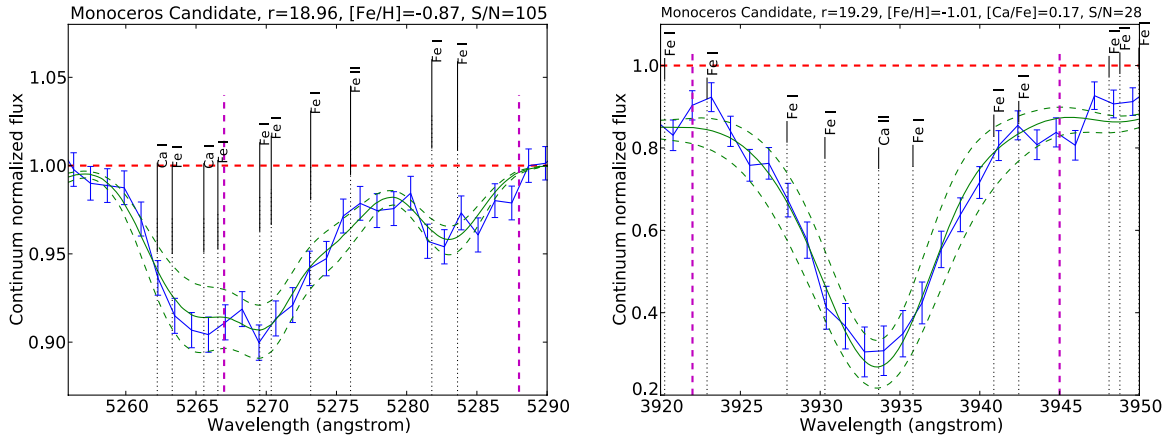


(a) (b)

**Figure 2.** (a) An example of the [Fe/H] fitting region for typical [Fe/H]. The blue line with error bars is the observed data, the green line is the best-fit synthetic spectrum, the red dashed line is the continuum fit, and the purple dashed lines show the fitting region boundary. The upper/lower green dashed lines show synthetic spectra with [Fe/H] lowered/raised by 0.25 dex relative to the best fit. The strong Fe I line at 5269.5 Å, plus the next nine most important lines by EW are marked with black vertical lines. (b) Same for Ca II K at 3933.7 Å, plus next 10 most important lines by EW, all of which are Fe I features. The upper/lower green dashed lines correspond to offsets in [Ca/Fe] of $\mp$0.25 dex relative to the best-fitting [Ca/Fe], keeping [Fe/H] fixed.

(A color version of this figure is available in the online journal.)

is typically ∼50–80 pixel$^{-1}$ at ∼5200 Å for the Monoceros stars and ∼135 for the brighter thick disk stars. We used the IRAF/rvsao routine `xcsao` to measure the radial velocity ($v_{\rm rad}$) of each star from cross-correlation with template stellar spectra on a per-exposure basis, correcting for heliocentric velocity before stacking the exposures of each object. Typical errors on $v_{\rm rad}$ ranged from 10 to 20 km s$^{-1}$, varying based on S/N.

### 2.3. Stellar Parameters

Abundance extraction requires estimates of several stellar parameters of each object, namely, the surface gravity log $g$, temperature $T_{\rm eff}$, microturbulence $v_t$, and metallicity. As our targets were selected from SDSS imaging, each star has $ugriz$ photometry available. Using I08 equation (3), which gives $T_{\rm eff}$ as a function of $g - r$, we determined effective temperatures for all program stars. The statistical error per star due to photometric errors is ∼80 K for thick disk targets and ∼110 K per star for the fainter Monoceros candidates. $T_{\rm eff}$ generally ranged from 5800 to 6300 K within each sample of Monoceros/thick disk stars.

Our targets were selected to be MSTO F/G dwarfs. Based on the stellar parameters of 46 dwarfs from Fulbright (2000) with $-2 \leqslant$ [Fe/H] $\leqslant 0.0$ and 5800 K $\leqslant T_{\rm eff} \leqslant$ 6300 K, we adopt $v_t = 1.25$ km s$^{-1}$ and log $g = 4.20$ for all Monoceros candidates and thick disk stars. In Section 3.5, we discuss the impact of these assumptions.

Of course, we wish to derive rather than assume metallicities. To extract abundances, we first determine [Fe/H] from iron absorption features assuming [X/Fe] = 0 for all X, choosing features where this assumption has negligible effect (see Figure 2(a) and Section 3.5). The [Fe/H] value of each object is then used as the metallicity input for subsequent Ca abundance measurements.

## 3. IRON ABUNDANCE OF THE MONOCEROS STREAM

To infer iron abundances from our spectra, we focus on the iron line complex near $\lambda \approx 5270$ Å. The absorption equivalent width (EW) in the region with 5267 Å $< \lambda <$ 5287 Å is dominated by Fe, mainly Fe I, but with some Fe II. The primary Fe lines of interest and major contaminating lines due to other elements are labeled in Figure 2(a). All abundances, including those drawn from the literature for calibration, were standardized with respect to the current solar values of Asplund et al. (2009).

### 3.1. Continuum Normalization

Given our relatively low resolution and moderate S/N, continuum normalization is a sensitive matter. We base our continuum fitting procedure on that used by the SEGUE Stellar Parameter Pipeline (SSPP; Lee et al. 2008) to measure [Fe/H], since our spectra have similar S/N and resolution to those for which their pipeline was designed. In particular, we iteratively fit the region of the spectrum blueward of 5800 Å with a ninth order polynomial, masking the strong Balmer lines. The SSPP additionally computes abundances with local continuum estimates based on sidebands. However, our resolution is a factor of ∼2 lower than that of SSPP spectra, making it unfeasible to isolate sideband regions which attain the continuum and are sufficiently wide to be robust.

### 3.2. [Fe/H] Fitting Technique

We take the calculated $T_{\rm eff}$ and assumed log $g$, $v_t$ for each star and compare the observed spectrum to a library of synthetic spectra generated based on these fixed stellar parameters, but with varying [Fe/H]. In particular, synthetic, continuum normalized spectra were generated using MOOG (the latest version, 2010; Sneden 1973), with one-dimensional no-overshoot model atmospheres (assuming local thermodynamic equilibrium) from Kurucz (1993). This version of MOOG accounts for the fact that Rayleigh scattering becomes an important source of continuum opacity at short wavelengths blueward of 4500 Å (Sobeck et al. 2011). For each [Fe/H] value with $-3.5 <$ [Fe/H] $< 0.5$ in gradations of 0.01 dex, we compute the $\chi^2$ between the synthetic spectrum and the observed, normalized spectrum over the Fe absorption region. We assign each star the [Fe/H] corresponding to the minimum $\chi^2$ value thus obtained. The $\chi^2$ is computed with the variance taken from Poisson statistics to be $\sigma^2 = (N/g + R^2)$, where $N$ is the counts per pixel in ADU, $R = 2.8$ ADU is the readnoise, and $g = 1$ is the gain. We compute the $\chi^2$ within the range 5267 Å $< \lambda <$ 5287 Å, a region

**Table 2**
Fe λ5269, Ca II K Line Lists

| Fe λ5269 | | | | Ca II K | | | | Ca II K cont'd | | | |
|---|---|---|---|---|---|---|---|---|---|---|---|
| λ (Å) | Species | E.P. (eV) | log $gf$ | λ (Å) | Species | E.P. (eV) | log $gf$ | λ (Å) | Species | E.P. (eV) | log $gf$ |
| 5268.6 | Ti II | 2.59 | −1.96 | 3922.1 | Fe I | 3.29 | −2.44 | 3933.3 | Sc I | 2.3 | −1.29 |
| 5268.9 | Ti I | 3.32 | −1.74 | 3922.7 | Fe I | 2.99 | −2.0 | 3933.4 | Sc I | 0.02 | −0.65 |
| 5269.5 | Fe I | 0.86 | −1.32 | 3922.9 | Fe I | 0.05 | −1.65 | 3933.6 | Fe I | 3.07 | −1.16 |
| 5269.9 | Ti I | 1.87 | −1.74 | 3923.0 | Sc I | 1.99 | −2.69 | 3933.6 | Fe I | 3.27 | −2.05 |
| 5270.3 | Ca I | 2.52 | 0.16 | 3923.0 | Fe I | 3.25 | −2.27 | 3933.7 | Ca II | 0.0 | 0.11 |
| 5270.4 | Fe I | 1.6 | −1.34 | 3923.5 | Sc II | 0.32 | −2.41 | 3933.9 | Ti I | 2.29 | −2.32 |
| 5271.6 | Ti I | 2.77 | −0.87 | 3924.5 | Ti I | 0.02 | −0.94 | 3934.2 | Ti I | 0.05 | −2.14 |
| 5272.0 | Cr I | 3.44 | −0.42 | 3925.2 | Fe I | 3.29 | −1.4 | 3935.3 | Fe I | 2.85 | −1.87 |
| 5273.2 | Fe I | 3.29 | −0.99 | 3925.6 | Fe I | 2.83 | −1.03 | 3935.8 | Fe I | 2.83 | −0.88 |
| 5273.4 | Fe I | 2.48 | −2.16 | 3925.8 | Sc I | 1.99 | −2.27 | 3935.9 | Fe I | 3.27 | −2.13 |
| 5273.4 | Cr I | 3.45 | −0.7 | 3925.9 | Fe I | 2.86 | −0.94 | 3936.3 | Ti I | 2.48 | −2.73 |
| 5274.4 | Ti I | 3.09 | −3.03 | 3926.0 | Fe I | 3.24 | −0.93 | 3936.5 | Sc I | 2.32 | −1.6 |
| 5274.6 | Ti I | 2.42 | −2.97 | 3926.3 | Ti I | 2.58 | −1.91 | 3936.8 | Fe I | 3.25 | −1.94 |
| 5275.2 | Cr I | 3.37 | −0.35 | 3927.7 | Sc I | 1.99 | −1.36 | 3937.0 | Ti I | 2.29 | −2.38 |
| 5275.3 | Cr I | 2.88 | −0.28 | 3927.8 | Sc I | 1.99 | −1.69 | 3937.3 | Fe I | 2.69 | −1.46 |
| 5275.8 | Cr I | 2.88 | −0.05 | 3927.9 | Fe I | 0.11 | −1.52 | 3937.6 | Ti I | 2.3 | −2.34 |
| 5276.0 | Fe II | 3.19 | −2.21 | 3927.9 | Fe I | 2.83 | −2.27 | 3937.7 | Fe I | 3.02 | −1.82 |
| 5276.1 | Cr I | 2.88 | −0.1 | 3928.1 | Fe I | 3.21 | −0.93 | 3937.9 | Ti I | 2.17 | −2.28 |
| 5277.0 | Ti I | 3.33 | −1.67 | 3928.8 | Ti I | 2.31 | −1.71 | 3938.0 | Ti I | 2.27 | −2.08 |
| 5278.2 | Sc I | 3.05 | −1.74 | 3929.0 | Ti I | 2.04 | −1.5 | 3938.6 | Sc I | 2.3 | −1.6 |
| 5278.2 | Ti I | 2.34 | −2.5 | 3929.0 | Ti I | 2.3 | −1.85 | 3938.6 | Sc I | 2.34 | −1.72 |
| 5278.3 | Sc I | 3.05 | −3.05 | 3929.1 | Fe I | 2.76 | −1.88 | 3939.7 | Ti I | 2.31 | −2.47 |
| 5279.7 | Fe I | 3.3 | −3.44 | 3929.2 | Fe I | 3.25 | −1.34 | 3940.0 | Sc I | 2.61 | −2.12 |
| 5280.3 | Cr I | 3.36 | −0.73 | 3929.9 | Ti I | 0.0 | −1.06 | 3940.1 | Ti I | 2.5 | −2.96 |
| 5281.8 | Fe I | 3.03 | −0.83 | 3930.2 | Sc I | 1.99 | −1.4 | 3940.9 | Fe I | 0.96 | −2.6 |
| 5282.4 | Ti I | 1.05 | −1.3 | 3930.2 | Ti I | 1.5 | −1.23 | 3941.3 | Fe I | 3.27 | −1.01 |
| 5283.4 | Ti I | 1.87 | −0.49 | 3930.3 | Fe I | 0.09 | −1.49 | 3941.4 | Sc I | 2.0 | −1.5 |
| 5283.6 | Fe I | 3.24 | −0.43 | 3930.5 | Fe I | 3.21 | −2.52 | 3942.4 | Fe I | 2.99 | −2.07 |
| 5284.1 | Fe II | 2.89 | −3.2 | 3930.9 | Fe I | 2.45 | −2.86 | 3942.4 | Fe I | 2.85 | −0.95 |
| 5284.4 | Ti I | 1.04 | −2.43 | 3931.1 | Ti I | 2.29 | −2.04 | 3942.8 | Fe I | 3.27 | −1.31 |
| 5285.0 | Sc I | 2.5 | −1.42 | 3931.1 | Fe I | 3.27 | −1.14 | 3943.3 | Fe I | 2.2 | −2.35 |
| 5285.6 | Cr I | 3.36 | −1.13 | 3931.3 | Fe I | 3.24 | −1.9 | 3943.7 | Sc I | 2.0 | −2.74 |
| 5285.8 | Sc I | 2.5 | 0.38 | 3931.6 | Ti I | 2.32 | −1.63 | 3944.3 | Sc I | 2.61 | −2.36 |
| ... | ... | ... | ... | 3932.0 | Sc I | 1.99 | −1.34 | 3944.4 | Ti I | 2.32 | −2.83 |
| ... | ... | ... | ... | 3932.0 | Ti II | 1.13 | −1.65 | 3944.7 | Fe I | 2.85 | −2.09 |
| ... | ... | ... | ... | 3932.6 | Sc I | 1.85 | −1.74 | 3944.9 | Fe I | 2.99 | −1.45 |
| ... | ... | ... | ... | 3932.6 | Fe I | 2.73 | −1.16 | ... | ... | ... | ... |

determined to optimize the Fe absorption relative to absorption by other elements and random noise. An example best-fit result for typical S/N and iron absorption strength is plotted in Figure 2(a). The line list employed in our syntheses is provided in Table 2.

### 3.3. Iron Abundance Calibration

To test our [Fe/H] fitting procedure, we apply the above methodology to 189 MMT/Hectospec spectra of globular cluster stars in M13 with comparable S/N and SDSS photometry. We again estimate $T_{\rm eff}$ from $g-r$ and adopt $v_t = 1.5$ km s$^{-1}$, log $g = 4.25$ based on Briley & Cohen (2001) Table 2. M13 is known to have [Fe/H] $= -1.55$ (Cohen & Meléndez 2005), and we recover a median [Fe/H] of $-1.51$. We thus apply a $-0.04$ dex correction factor to all of our [Fe/H] measurements.

### 3.4. Rejecting Poorly Determined [Fe/H]

Based on visual inspection of the faintest and apparently most metal-poor objects in our Monoceros candidate sample, it became clear that several of these lacked sufficient iron EW to measure [Fe/H] in the presence of statistical noise and minor continuum placement errors. To remove these outliers, we computed $\sigma_{\rm EW}$, the $1\sigma$ error in total Fe fitting region EW due to Poisson noise and continuum placement errors. The continuum error was estimated by fitting a polynomial two orders lower than the default continuum, and generally amounted to <1% continuum level difference. We then rejected all stars for which the S/N and EW were sufficiently low that $\sigma_{\rm EW}$ translated to >0.5 dex [Fe/H] uncertainty. For Monoceros targets in the fields NORTH, SOUTH, and NORTH18, the percentage of stars rejected was 7.5%, 6.8%, and 0.4%, respectively. All rejected stars had estimated [Fe/H] $< -2.05$. No thick disk [Fe/H] estimates were rejected, as these stars generally have higher S/N and metallicity than the Monoceros candidates.

In performing maximum likelihood fits to our [Fe/H] distributions (see Section 3.6) we also identified, among Monoceros candidates, three [Fe/H] outliers at [Fe/H] > 0. These objects also displayed unreasonably low [Ca/Fe] $< -1$, again suggesting a dramatic overestimate of [Fe/H]; these three objects were also excluded from the sample.

### 3.5. Iron Abundance Uncertainties

There are several uncertainties on our derived metallicities. First there is statistical scatter from Poisson noise, which, for

typical S/N is a function of [Fe/H]. We gauge this error with Monte Carlo generation of spectra to which we have added random Poisson noise. For typical [Fe/H] $= -1$, we find an rms scatter of 0.11 dex. At typical halo [Fe/H] $= -1.6$ we find a scatter of 0.25 dex, while for typical thick disk [Fe/H] $= -0.7$ we find an rms scatter of only 0.05 dex. With sample sizes of 100–250 stars per field, this statistical error is thus not a primary concern.

Another source of uncertainty stems from our assumptions about stellar parameters. We find the effects of reasonably large systematic over/underestimates in each of log $g$ ($\pm 0.3$ dex), $T_{\rm eff}$ ($\pm 100$ K), and $v_t$ ($\pm 0.3$ dex), to be $\mp 0.05$ dex, $\pm 0.07$ dex, $\pm 0.07$ dex in [Fe/H], respectively. Summing these effects in quadrature yields an uncertainty of $\pm 0.11$ dex on our derived metallicities.

A further possible source of bias in [Fe/H] is contamination of the iron abundance fitting region by lines of other elements, most notably Ca (see Figure 2(a)). In determining [Fe/H], we generated synthetic spectra assuming that [X/Fe] $= 0$ for all X. While [X/Fe] is not known for Monoceros, the most relevant parameter of [Ca/Fe] for the Galactic disk/halo tends to lie between 0.0 and 0.4. We address the resulting [Fe/H] bias by using MOOG to simulate populations of stars with [Ca/Fe] following the known Galactic trend with [Fe/H] (see Section 4.1), adding appropriate noise to the synthetic spectra before feeding them back into our [Fe/H] fitter. The resulting bias is very small, $\lesssim 0.02$ dex.

A final important source of uncertainty is the continuum normalization procedure. With our low resolution, the blending of lines means the continuum is rarely achieved, and could potentially be systematically over/underestimated throughout the sample, thereby raising/lowering all metallicities. To test the systematic effect due to differing continuum normalizations, we again re-fit abundances with new continua parameterized by a polynomial two orders lower than the default continuum. We find in general a resulting systematic offset of 0.07 dex in [Fe/H].

We assign a final systematic uncertainty of 0.13 dex to our [Fe/H] distributions, adding the errors from continuum fitting and stellar parameters in quadrature. This value is somewhat conservative, as much of this uncertainty (particularly the continuum normalization) has been calibrated out with the M13 data. We find, through simulations similar to those previously described, that the observed [Fe/H] scatter is well described by a combination of both Poisson noise and statistical scatter of the underlying stellar parameters, again at the level of $\pm 100$ K in $T_{\rm eff}$, $\pm 0.3$ dex in both $v_t$ and log $g$. Thus, summing these sources of scatter in quadrature, we find for typical S/N and [Fe/H] $= -1$ a single-star statistical error of 0.16 dex.

### 3.6. Decomposing the [Fe/H] Distributions

To characterize the Monoceros MDF, we must first decompose the distribution of reliable [Fe/H] estimates in each field into Galactic components (halo, disk) and Monoceros members. To estimate the expected background in both halo and disk stars, we simulate CMDs for each pointing with both the Besançon model (Robin et al. 2003) and *galfast*, using the best-fit Galactic parameters of Jurić et al. (2008). All simulations included realistic photometry errors and were extinction free, for comparison to observed SDSS CMDs dereddened according to Schlegel et al. (1998, hereafter SFD). We created a matched filter in target density for the stars with reliable [Fe/H] in each field, then integrated against the observed, Besançon and *galfast* star counts to determine the expected number of contaminating stars from the disk and halo. For each field, overall CMD normalization constants close to unity were applied by requiring agreement between the total number of stars redder than $g - r = 0.8$ and falling within the targeted range of $r$ values. This analysis suggests $\sim$65% of Monoceros candidates with well-measured [Fe/H] are true stream members. In no case do we expect any thin disk stars, as the Monoceros targets have $|Z| \geqslant 2.5$ kpc.

Figure 3 shows a decomposition of the observed distributions of reliable [Fe/H] for each field. In principle, there are nine free parameters: the normalization of Monoceros, thick disk, and halo components, their median metallicities, and their dispersions. The following subsections describe our assumptions for the thick disk and halo distributions and procedure for fitting the Monoceros component.

#### 3.6.1. Thick Disk Parameters

In each field, the thick disk normalization was fixed by the CMD analysis to be the average of the predictions from the *galfast* and Besançon simulations. In fields NORTH and SOUTH we fix the median metallicity to that of the thick disk targets in these fields, plus a small $-0.02$ dex correction from Bond et al.'s (2010) equation (A2) to account for the vertical disk metallicity gradient (our thick disk targets are at lower $|Z|$ than the more distant thick disk stars which contaminate the Monoceros sample). For field NORTH18, in which we did not target any thick disk stars, the median [Fe/H] used for field NORTH was adopted. A 0.35 dex intrinsic dispersion calculated from the kinematically selected thick disk stars in Bensby et al. (2007) was adopted for the thick disk in all fields.

#### 3.6.2. Halo Parameters

In fields NORTH and NORTH18, the halo normalization was fixed to the average of the *galfast* and Besançon predictions. A cut on $|v_{\rm rad}| > 150$ km s$^{-1}$, yielding a subsample which should be dominated by large velocity dispersion halo members, suggests that the absolute number of halo stars in each field is roughly constant. However, in field SOUTH, *galfast* gives an unreasonably large halo contribution relative to this expectation, so in that case we simply use the Besançon value. For field NORTH18, the halo median/dispersion were fit by examining the top quartile of stars in S/N (62 stars, S/N $> 96$), which displayed a relatively narrow peak at [Fe/H] $= -1.57$. For field NORTH, we used SDSS proper motions from Munn et al. (2004) to isolate seven halo stars with the cut $|v_{\rm rad}| > 100$ km s$^{-1}$ and $\mu_l > 220$ km s$^{-1}$. This yielded a median metallicity of $-1.80$. For field SOUTH, the kinematic data were of lower quality, and we adopt [Fe/H] $= -1.6$ from Carollo et al. (2010). For fields NORTH and SOUTH the dispersion was calculated by adding the errors due to Poisson noise and stellar parameter scatter in quadrature with a 0.3 dex intrinsic halo [Fe/H] dispersion (I08).

#### 3.6.3. Fitting Monoceros Parameters

The normalization of the Monoceros distribution is fixed by requiring that the components sum to the total number of targets. This leaves two free parameters characterizing the Monoceros MDF: its median and dispersion. All components were assumed to be intrinsically gaussian. To account for detection inefficiency at very low [Fe/H], we modulated the distributions by a linear ramp defined to be zero at (and below) the minimum detected [Fe/H] and unity at (and above) the maximum rejected [Fe/H]. For each field, we fit the Monoceros [Fe/H] median $\mu_{\rm mon}$ and

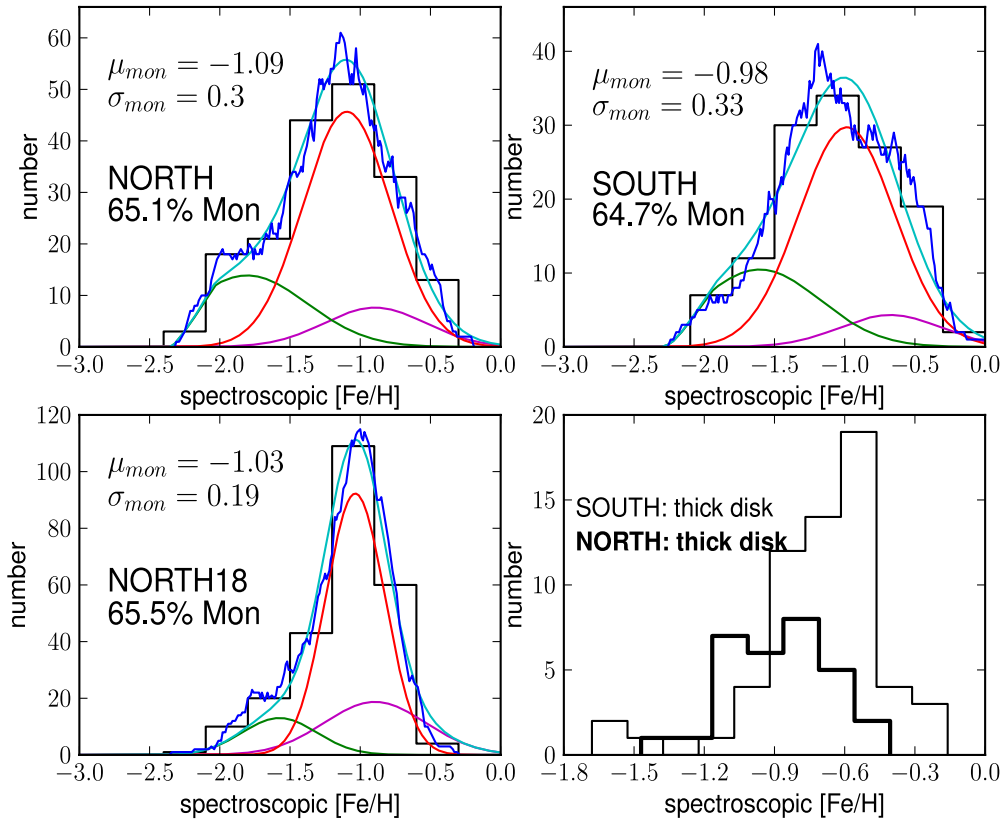


**Figure 3.** Top row, bottom left: decompositions of the $[Fe/H]_{spec}$ distributions for each of our three Monoceros target fields. In each case, the green line represents the assumed halo contribution, the purple line represents the assumed thick disk contribution, the red line represents the best-fit Monoceros contribution, and the cyan line gives the sum of these three components. The black histogram shows the observed $[Fe/H]_{spec}$ distribution in bins 0.3 dex wide, while the blue line is a curve which counts the number of objects within a 0.3 dex wide [Fe/H] bin, as the bin center is shifted incrementally by 0.01 dex at a time. Bottom right: $[Fe/H]_{spec}$ distributions of thick disk targets in Galactic north (thick black line) vs. south (thin black line) displaying the observed 0.22 dex metallicity asymmetry.

(A color version of this figure is available in the online journal.)

**Table 3**
[Fe/H] Distribution Fitting Assumptions/Results

| Field | $N_{stars}$ | $N_{halo}$ | $N_{TD}$ | $N_{mon}$ | [Fe/H] $\mu_{TD}$ | $\sigma_{TD}$ (dex) | $\mu_{halo}$ | $\sigma_{halo}$ (dex) | $\mu_{mon}$ | $\sigma_{mon}$ (dex) |
|---|---|---|---|---|---|---|---|---|---|---|
| NORTH | 183 | 40.7 | 23.2 | 119.2 | −0.89 | 0.35 | −1.80 | 0.42 | −1.09 | 0.30 |
| SOUTH | 131 | 33.3 | 13.0 | 84.7 | −0.67 | 0.35 | −1.60 | 0.42 | −0.98 | 0.33 |
| NORTH18 | 247 | 28.7 | 56.4 | 161.8 | −0.89 | 0.35 | −1.57 | 0.25 | −1.03 | 0.19 |

dispersion $\sigma_{mon}$ by maximizing the likelihood:

$$L = \frac{1}{n}\sum_{i=1}^{n} \log_{10}\{P([Fe/H]_i; \mu_{mon}, \sigma_{mon})\}, \quad (1)$$

where $n$ is the total number of reliable [Fe/H] measurements in each field and $P([Fe/H])$ is the normalized sum of the halo, thick disk, and trial Monoceros modulated Gaussian distributions. Table 3 lists the fitting assumptions and results, which agree with expectations based on visual inspection.

## 4. CALCIUM ABUNDANCE OF THE MONOCEROS STREAM

We have also measured [Ca/H] using the Ca II K line for program stars sufficiently metal-poor to avoid saturation effects ([Fe/H] $< -0.5$). Our [Ca/H] determination follows a procedure very similar to that described for [Fe/H] in Section 3.2. For each star, we adopt the same stellar parameters as in the [Fe/H] fits, but now input the measured [Fe/H] as the Kurucz atmosphere metallicity. To determine each star's [Ca/H] value, we minimize the same $\chi^2$ statistic, this time for $3922\,\text{Å} < \lambda < 3945\,\text{Å}$. The line list for Ca II K syntheses is provided in Table 2.

### 4.1. Continuum Normalization and Calcium Calibration

For the Ca fitting region, we used a local continuum normalization procedure, iteratively fitting a second-order polynomial to the region $3845\,\text{Å} < \lambda < 4045\,\text{Å}$. We found that this continuum essentially matched the values/slopes of the continuum on the two "sideband" regions blueward/redward of the Ca II H/K absorption. This fits the continuum shape well, but underestimates the normalization by neglecting absorption which causes the continuum to be rarely if ever realized. For this reason, these continuum fits caused [Ca/H] to be systematically underestimated, with the effect becoming more pronounced with increasing [Fe/H].

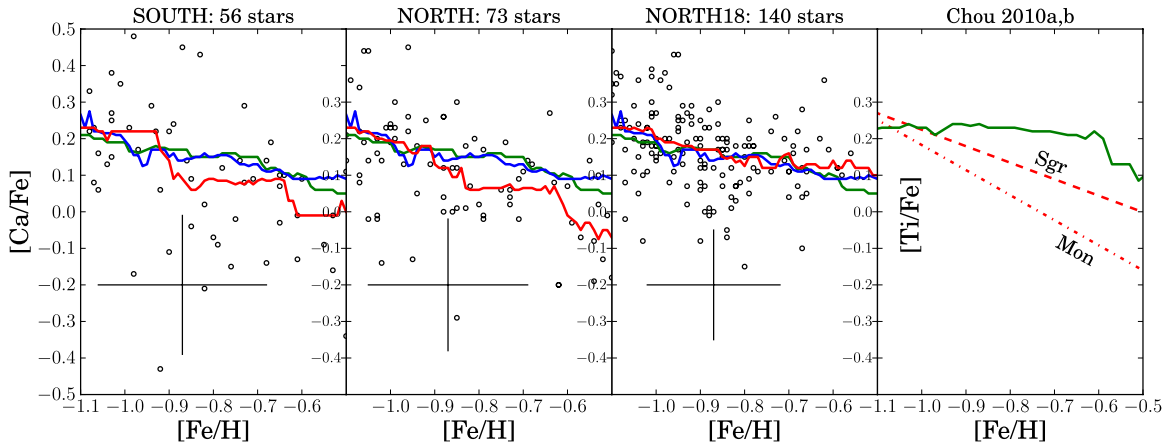


**Figure 4.** Leftmost three panels: [Ca/Fe] as a function of [Fe/H] for Monoceros fields. The green line is the Galactic trend from Gratton et al. (2003), the blue line represents our thick disk sample, and the red line represents Monoceros candidates. All lines are constructed by taking the median of individual measurements in bins 0.2 dex wide in [Fe/H] centered about the abscissa. Open circles are measurements for individual stars, and the crosses indicate typical single-star error bars at the low-metallicity end, [Fe/H] = −1.1. Rightmost panel: the green line shows the [Ti/Fe] trend inferred from Gratton et al. (2003) in a fashion identical to that used to construct the green [Ca/Fe] lines at left. The dot-dashed and dashed red lines give linear fits to [Ti/Fe] measurements of 21 Monoceros members and 70 Sagittarius stream members, respectively (Chou et al. 2010a, 2010b). Two of three Monoceros fields (NORTH and SOUTH) show [Ca/Fe] underabundance trends relative to the Milky Way similar to those displayed by [Ti/Fe] in Sgr and Mon.

(A color version of this figure is available in the online journal.)

We recalibrate the continuum by requiring that our thick disk sample exhibit a trend of [Ca/Fe] versus [Fe/H] matching that from the literature. The expected trend was computed using 150 Milky Way field stars from Gratton et al. (2003). We found that good agreement in slope could be achieved by multiplying the initial continua by a factor of $(1 + \delta)$, with $\delta$ increasing linearly from zero at low metallicity, $[\mathrm{Fe/H}]_{\mathrm{M13}} = -1.55$, to 13% at [Fe/H] = −0.50. Agreement in offset was achieved with subsequent addition of 0.03 dex to all [Ca/Fe]. Applying this procedure to our 189 M13 spectra yielded [Ca/Fe] = 0.25, in agreement with the estimate of Cohen & Meléndez (2005), who find [Ca/Fe] = 0.19 ± 0.07 from high-resolution spectroscopy of 25 cluster members.

We apply the local continuum fit and subsequent recalibration to Monoceros candidates with $-1.1 < [\mathrm{Fe/H}] < -0.5$, where we had sufficient disk stars to verify the recalibration procedure. Figure 4 overplots these Monoceros results with the literature trend and recalibrated disk, where the lines are constructed by taking the median of [Ca/Fe] in bins 0.2 dex wide in [Fe/H]. Also plotted are linear fits to recent [Ti/Fe] abundances of 70 Sagittarius and 21 Monoceros stream members (Chou et al. 2010a, 2010b). The $\alpha$-enhancements [Ti/Fe] and [Ca/Fe] are expected to display similar trends, as both reflect the relative heavy element contributions of Type II ($\alpha$-elements + Fe) versus Type Ia supernovae (Fe only), and hence probe the star formation history. dSph galaxies typically show deficiencies in $\alpha$-elements relative to the Milky Way, owing to a slower star formation rate in which fewer Type II explosions occur before the onset of Type Ia explosions at $\geqslant$1 Gyr.

## 5. DISCUSSION

### 5.1. Monoceros Abundances

As the Monoceros members comprise ∼2/3 of targets in each field, it can be seen by visual inspection that Monoceros has a median [Fe/H] ∼ −1, distinct from both the thick disk and halo. Indeed, our maximum likelihood fits yield [Fe/H] ∼ −1.0 for each subsample, showing no trend with $l$ (see Table 3). I08 analyzed ∼11,000 MSTO stars in a similar spatial region to that of our targets ($13 < R_{\mathrm{GC}}/\mathrm{kpc} < 16$, $3 < Z/\mathrm{kpc} < 4$, $170^\circ < l < 190^\circ$; see their Figure 18); our inferred Monoceros medians $-1.09 < [\mathrm{Fe/H}] < -0.98$ are consistent with the I08 photometric estimate of [Fe/H] = −0.95 to within the systematic uncertainty of ∼0.13 dex on our spectroscopic abundances. It should be noted that we have used the same $g - r$ temperature calibration as I08. A more stringent test of SDSS photometric metallicities would be provided by a study deriving $T_{\mathrm{eff}}$ independently. See Section 5.3 for a detailed comparison of photometric versus spectroscopic metallicities.

I08 also inferred a small intrinsic Monoceros [Fe/H] dispersion of only 0.15 dex. For each field, we simulated the distributions of [Fe/H] arising from a monometallic population at $[\mathrm{Fe/H}] = \mu_{\mathrm{mon}}$, given our S/N distribution, $T_{\mathrm{eff}}$ distribution, continuum placement errors, and expected stellar parameter scatter. We found an rms measurement-induced scatter of 0.21 dex, 0.23 dex, and 0.16 dex for fields NORTH, SOUTH, and NORTH18, implying intrinsic scatters of 0.21 dex, 0.22 dex, 0.10 dex, respectively. Applying the same methodology to M13 stars of comparable S/N (>29), we find a measurement error of 0.36 dex, and observed scatter of 0.42 dex, yielding an intrinsic M13 scatter of 0.20 dex. Globular clusters generally have rms iron abundance dispersions $\leqslant$0.05 dex (Carretta et al. 2009). However, with only a single exposure, the M13 sample is subject to additional sources of error (e.g., cosmic rays) which we have not modeled, perhaps reconciling this difference. If we are indeed slightly underestimating the observation-induced scatter, a very conservative interpretation would regard the intrinsic Monoceros dispersions we obtained as upper limits.

For fields NORTH and NORTH18, a single Gaussian component is sufficient to describe the Monoceros MDF. For field SOUTH, there appears to be an excess at [Fe/H] ∼ −1.2. This could arise from a multimodality in the Monoceros MDF or, more likely, indicates contamination by the metal weak thick disk (MWTD; see Section 6.2). Inspection of the CMD in field SOUTH also suggests multiple main-sequence turnoffs aside from that of the disk. Given these uncertainties in population modeling, the inferred gradient in Monoceros median metallicity with $b$ (+0.11 dex from $b = +25^\circ$ to $b = -25^\circ$) appears not to be significant.

In two of three fields, the Monoceros [Ca/Fe] dips below the Galactic trend as [Fe/H] increases from −1.1 to −0.5 (see Figure 3). In fields NORTH and SOUTH, this [Ca/Fe] trend is qualitatively similar to the recently measured [Ti/Fe] trends of Monoceros and Sagittarius stream members (Chou et al. 2010a, 2010b). In field NORTH18, the observed Monoceros trend appears to exactly match that of the Milky Way. However, the field NORTH18 decomposition in Figure 3 suggests the measured [Fe/H] distribution cuts off more sharply than expected at high metallicity. If indeed [Fe/H] has been systematically underestimated for the highest metallicity stars in this field, [Ca/Fe] would be artificially inflated. It should be noted that our Monoceros sample plotted is a mixture of Monoceros and disk stars, driving down the apparent contrast between the Monoceros and Milky Way trends.

### 5.2. Thick Disk Abundances

In addition to the Monoceros candidates, in fields NORTH and SOUTH we measured [Fe/H] for 30 and 60 thick disk stars, respectively. These fields exhibit a strong stellar number density asymmetry, with the southern field showing an excess of more than 50% compared to its northern counterpart. The asymmetry is easily detected in the SDSS data, is also detectable in Pan-STARRS1 $3\pi$ survey data, and cannot be accounted for by photometric errors or reddening uncertainties. M. Jurić et al. (in preparation) speculate it may be a signature of yet another, more nearby, stream, or otherwise a global disturbance (a "warp" or a "bend") in the thick disk, of uncertain origin.

Figure 3 shows the measured distributions; the median and dispersion of [Fe/H] in field SOUTH are −0.65, 0.22 dex, respectively, while for field NORTH, the corresponding values are −0.87, 0.29 dex. The statistical scatter in our [Fe/H] measurements ∼0.05 dex per star has negligible effect on these values. The median $|Z|$ for the NORTH and SOUTH thick disk targets is, respectively, 1.60 kpc and 1.79 kpc, using the photometric parallax relation of I08 equations (A6) and (A7). According to the gradient in disk metallicity from Bond et al. (2010), this corresponds to an expectation, given perfect disk symmetry, that SOUTH would have [Fe/H] 0.01 dex *lower* than NORTH. The asymmetry is not simply reflecting different scale heights. Although the adopted systematic error on our metallicities is nominally 0.13 dex, this represents an offset with respect to the true abundances; our internal consistency should be much better, especially for these two thick disk samples which have very similar colors and S/N, as well as relatively strong Fe features. Reconciling the median metallicities of NORTH/SOUTH thick disk sample would require that stellar parameters such as log $g$ and $v_t$ differ greatly between the two populations, which itself would require invoking disk asymmetry about the midplane. A Kolmogorov–Smirnov test between the two measured [Fe/H] distributions yields a consistency probability of $<2.5 \times 10^{-3}$, even excluding the added 0.01 dex contrast from the $|Z|$ gradient in [Fe/H].

The dispersion in [Fe/H] for field SOUTH is 0.22 dex versus 0.29 dex for field NORTH and 0.35 dex for the thick disk (averaged over many directions) according to Bensby et al. (2007). A disrupted dSph origin for the overdensity would naturally explain the lower [Fe/H] dispersion in field SOUTH, but would also incorrectly predict an [Fe/H] lower than that of the northern disk for the southern stellar overdensity.

Thus, we have spectroscopically identified an asymmetry in the thick disk toward the Galactic anticenter, at $R_{GC} \approx 12$ kpc and $|Z| \approx 1.7$ kpc, which we expect to be confirmed and characterized further via stellar counts analysis.

### 5.3. Comparison with Photometric Metallicities

With $ugriz$ photometry available, we can compute $[Fe/H]_{phot}$ from Equation (A1) of Bond et al. (2010) for the entire sample. $[Fe/H]_{phot}$ is reddening sensitive. Schlafly & Finkbeiner (2010) have recalibrated SFD, finding the need for a substantial, ∼45%, global change in $E(u-g)$, but only a 2% change in $E(g-r)$. Thus, our $T_{eff}$ are negligibly affected at a $\lesssim$10 K level. But for fixed $g-r$, and near $[Fe/H]_{phot} = -1$, $[Fe/H]_{phot}$ has a strong $u-g$ gradient, >0.04 dex per 0.01 mag $u-g$. The Schlafly & Finkbeiner (2010) recalibration implies $\Delta(u-g) > 0.06$ in portions of our sample, a major effect. However, the $[Fe/H]_{phot}$ estimator of Bond et al. (2010) is tied to SFD reddenings, and we therefore calculate $[Fe/H]_{phot}$ using $(u-g)_{SFD}$; it may be necessary to revise the SDSS $[Fe/H]_{phot}$ relation using updated $E(u-g)$ values if these photometric metallicities are to be independent of dust column.

Furthermore, single-pointing samples of $[Fe/H]_{phot}$ and $[Fe/H]_{spec}$ are sensitive to local reddening in differing ways ($[Fe/H]_{spec}$ is a function of $g-r$ reddening through $T_{eff}$). Near [Fe/H] = −1, using conventional reddening laws, overestimating $A_r$ leads to an underestimate of $[Fe/H]_{phot}$, but to an overestimate of $[Fe/H]_{spec}$ for fixed absorption EW. Any local (degree scale) error in $A_r$ drives our photometric and spectroscopic metallicities apart.

Nevertheless, we find a highly significant correlation between $[Fe/H]_{phot}$ and $[Fe/H]_{spec}$. The correlation is strongest for the highest S/N spectra, corresponding to the brightest objects with least noisy $ugr$ photometry and best measured $[Fe/H]_{spec}$. M13, closely approximating a monometallic population, shows only a marginal correlation, in accordance with the expectation that the observed spread in [Fe/H] values arises predominantly from random scatter in the photometric/spectroscopic measurements.

Figure 5 overplots the distributions of photometric/spectroscopic metallicities for each of our subsamples. In general, the median photometric and spectroscopic metallicities agree at the level of ∼0.15 dex, which can be reconciled by the estimated systematic uncertainties of 0.13 dex on $[Fe/H]_{spec}$ and 0.1 dex on $[Fe/H]_{phot}$ (I08). Except for the M13 sample, the $[Fe/H]_{spec}$ distributions are narrower than their $[Fe/H]_{phot}$ counterparts by a median of 0.07 dex in dispersion. Of course, much of the total dispersion is intrinsic. The superiority of M13 $[Fe/H]_{phot}$ owes to the targets being relatively bright ($r \sim 18$), yielding good photometry, yet receiving only a single, short Hectospec exposure.

### 5.4. Radial Velocities

As a byproduct of our abundance extraction procedure, we have heliocentric radial velocities in hand for our entire sample. Typical statistical errors are 10–20 km s$^{-1}$, depending on S/N. We gauged our systematic error using M13 as a calibration sample, since this globular cluster has a known $v_{rad} = -244.2$ km s$^{-1}$ (Harris 1996). We find for our 189 M13 spectra a median of $v_{rad} = -241.1$ km s$^{-1}$, and therefore have applied a correction of −3.1 km s$^{-1}$ to all radial velocity measurements.

#### 5.4.1. Monoceros Candidates

Y03 found that Monoceros is kinematically cold, consistent with the expectation for a disrupted dSph galaxy, measuring radial velocity dispersions $\sigma_r = 22$–30 km s$^{-1}$. For stars with

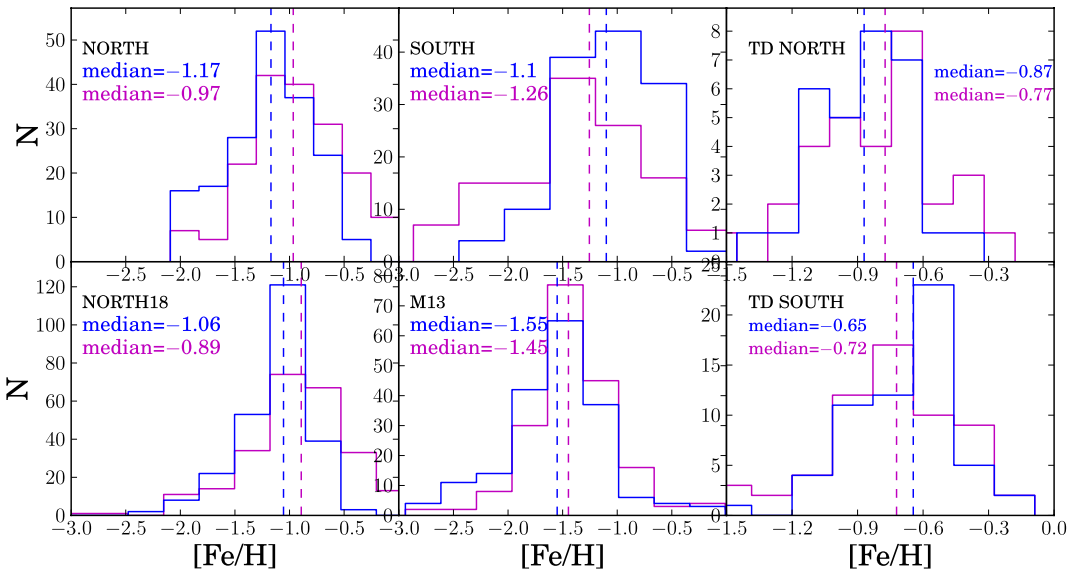


**Figure 5.** Photometric (magenta) vs. spectroscopic (blue) [Fe/H] distributions. The distributions generally agree at the level of ∼0.15 dex, which can be accounted for by the estimated 0.13 dex systematic error on our spectroscopic metallicities and the 0.1 dex systematic error on $[Fe/H]_{phot}$. In general, the photometric metallicity distributions are slightly broadened relative to the spectroscopic distributions.

(A color version of this figure is available in the online journal.)

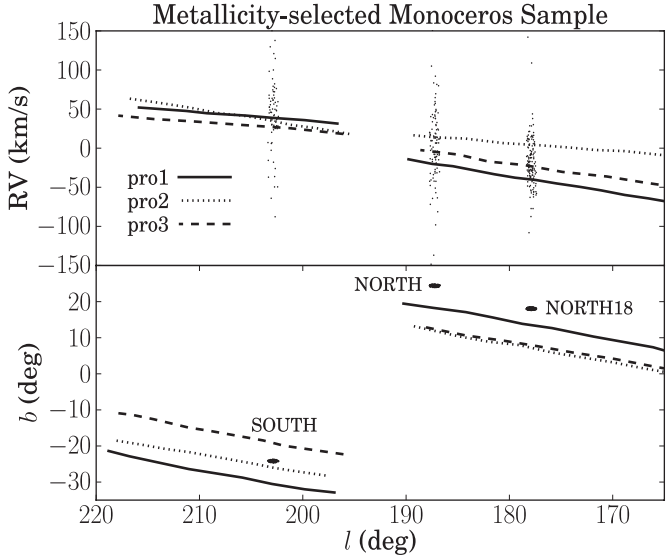


**Figure 6.** Adaptation of Peñarrubia et al. (2005), their Figure 7. Bottom: prograde orbit models (pro1, pro2, pro3) of Monoceros debris position in the anticenter direction. The gap at $l \sim 195°$ signifies that field SOUTH corresponds to a different orbital "wrap" than NORTH and NORTH18. Top: model-predicted radial velocity as a function of galactic longitude, with each point representing a star in our metallicity-selected Monoceros sample.

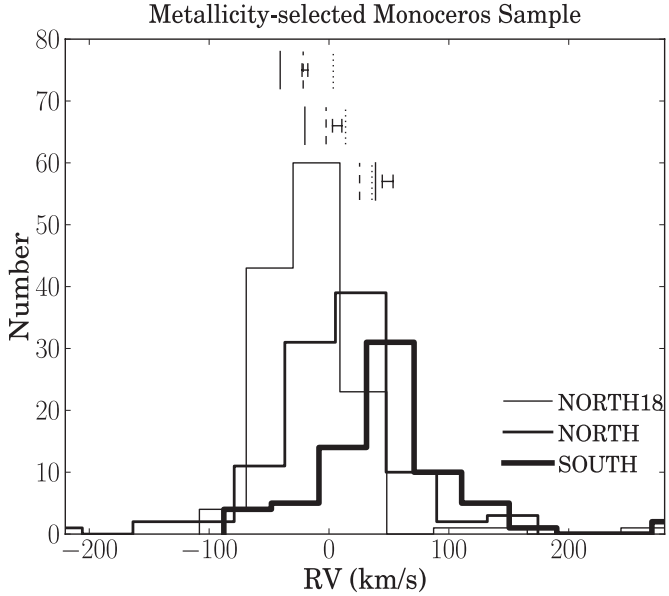


**Figure 7.** Histograms of metallicity-selected Monoceros candidate radial velocities by field. Capped, solid horizontal lines represent measured $v_{rad}$ medians and their standard errors. Corresponding (uncapped) vertical lines represent the model predictions at each field location, with the same line-type legend as in Figure 6.

$\mu_{mon} - \sigma_{mon} \leqslant [Fe/H] \leqslant \mu_{mon} + \sigma_{mon}$ in fields NORTH, SOUTH, and NORTH18, we find $\sigma_r = 35.7, 31.3, 26.3$ km s$^{-1}$ after correcting for median measurement uncertainties of 17, 24, 11 km s$^{-1}$, respectively. For comparison, the *galfast* (Besançon) predictions for $\sigma_r$ of thick disk stars in these fields is 57.7 (38.4), 56.6 (36.3), 54.3 (35.8) km s$^{-1}$. All dispersions were calculated as half of the difference between the 84th and 16th percentile $v_{rad}$ values. In all cases, the metallicity-selected Monoceros sample is kinematically cold relative to the thick disk model, and appreciably so if we to are to adopt the *galfast* prediction. Our range of $\sigma_r$ is slightly higher than that found by Y03 but this may be due to contamination of the sample by disk and halo stars, both of which would tend to increase $\sigma_r$.

We can also compare the median $v_{rad}$ for the metallicity-selected Monoceros samples to the predictions of Peñarrubia et al. (2005). Figure 6 overplots measured radial velocities with the three prograde orbit models of Peñarrubia et al. (2005). Figure 6 also plots $l$ versus $b$ for our Monoceros targets and the Peñarrubia et al. (2005) orbits, showing that field SOUTH is on a different "wrap" of the stream than are NORTH and NORTH18.There is indeed qualitative agreement between all of the models and our measured median $v_{rad}$ for NORTH, SOUTH, and NORTH18 of $7 \pm 2.9$, $49 \pm 4.5$, $-20 \pm 2.4$ km s$^{-1}$, trending upward with increasing $l$. Quantitative agreement is only achieved at the ∼10 km s$^{-1}$ level, with no single model

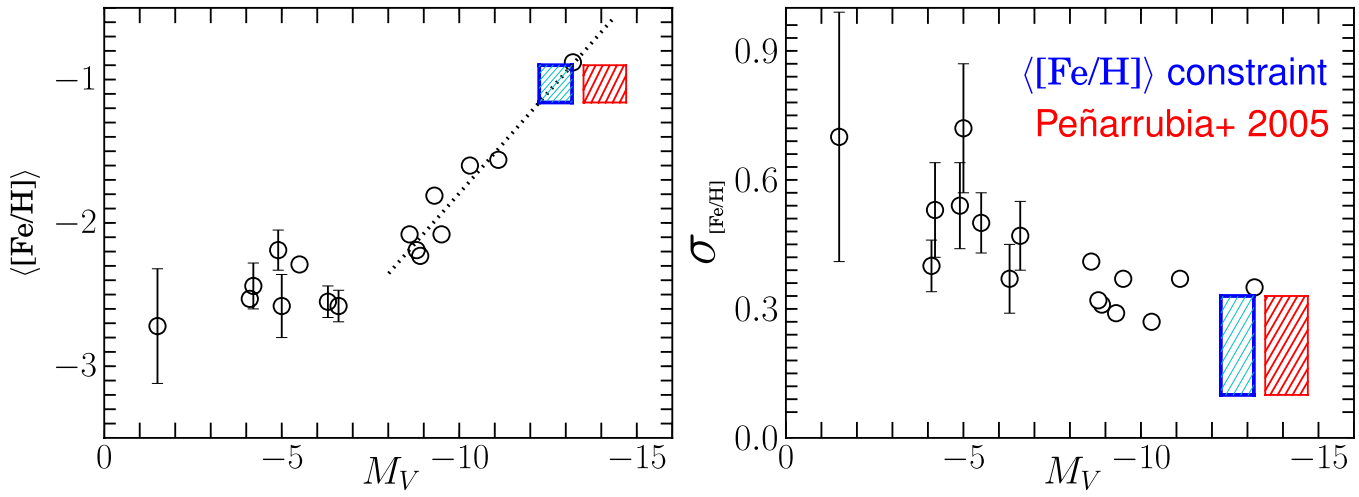


**Figure 8.** Left: ⟨[Fe/H]⟩ vs. $M_V$, where each circle represents a single dwarf galaxy, with properties quoted from Norris et al. (2010) and references therein. Error bars are only shown when the uncertainty on ⟨[Fe/H]⟩ exceeds 0.1 dex. The dashed line shows our linear fit to the eight plotted galaxies brighter than $M_V = -8$. The blue rectangle represents the allowed region of parameter space, combining this computed trend with our measured MDF, and constrains the Monoceros progenitor to have $-13.2 \leqslant M_V \leqslant -12.3$. Alternatively, we can use the Monoceros progenitor mass estimated by Peñarrubia et al. (2005) and assume the Sgr mass-to-light ratio to plot our Monoceros MDF (red hatched rectangle). Clearly, Monoceros follows the general dwarf galaxy trend of increasing ⟨[Fe/H]⟩ with increasing luminosity. Right: $\sigma_{[Fe/H]}$ vs. $M_V$. Circles are individual dwarf galaxies with properties drawn from Norris et al. (2010) and references therein. Error bars are only shown when the uncertainty on $\sigma_{[Fe/H]}$ exceeds 0.05 dex. Again, we have plotted Monoceros as the red hatched rectangle by assuming the Peñarrubia et al. (2005) mass and Sgr mass-to-light ratio, and as a blue hatched rectangle using the ⟨[Fe/H]⟩ constraint on $M_V$. Monoceros also follows the dwarf galaxy trend of decreasing $\sigma_{[Fe/H]}$ with increasing luminosity.

(A color version of this figure is available in the online journal.)

particularly favored, as shown by the histograms of the metallicity-selected Monoceros $v_{rad}$ measurements in each field (Figure 7). The median Monoceros $v_{rad}$ values generally differ substantially from the *galfast* (Besançon) thick disk $v_{rad}$ predictions of 30 (22), 54 (59), 5 (6) km s$^{-1}$ for fields NORTH, SOUTH, and NORTH18, respectively. In summary, the measured radial velocities of our metallicity-selected Monoceros subsamples are kinematically cold relative to the thick disk, have different median values than expected for thick disk stars, and generally agree with the model predictions of Peñarrubia et al. (2005).

#### 5.4.2. Thick Disk Targets

Since, as discussed in Section 5.2, we find that the thick disk SOUTH sample is chemically distinct from its northern counterpart, it is of interest to compare the measured thick disk radial velocities with *galfast*/Besançon predictions. For both the NORTH and SOUTH thick disk samples, we find rather poor agreement in terms of median $v_{rad}$, with measured values of $-8$, 31 km s$^{-1}$ versus *galfast* (Besançon) predicted values of 21 (18), 52 (49) km s$^{-1}$. The measured dispersions $\sigma_r$ for NORTH and SOUTH are 42, 25 km s$^{-1}$ versus *galfast* (Besançon) predicted values of 46 (47), 46 (49) km s$^{-1}$. The measured velocity dispersion in field NORTH agrees with the thick disk predictions, whereas the SOUTH targets are much more kinematically colder than expected. Thus, the thick disk kinematics also display a north/south asymmetry, with a low velocity dispersion for the southern overdensity suggestive of a coherent stream.

## 6. CONCLUSIONS

### 6.1. What is the Monoceros Iron Abundance?

We have presented the first ever spectroscopic Monoceros MDF based directly on Fe absorption line measurements, finding [Fe/H] $= -1.0 \pm 0.1$. Our results confirm the photometric metallicity analyses of I08 ([Fe/H] $= -0.95$) and Sesar et al. (2011), who also used the Bond et al. (2010) calibration to derive results consistent with [Fe/H] $\sim -1.0$ toward $(l,b) = (232^\circ,26^\circ)$. However, these earlier results are vulnerable to systematic problems (e.g., $u$-band extinction uncertainties) which are largely circumvented by our spectroscopic analysis.

While C03 and Y03 inferred [Fe/H] for Monoceros spectroscopically, neither measured Fe absorption directly. Instead, both relied upon indices calibrated to Mg and Ca features. Our [Ca/Fe] results suggest that such calibrations of [Fe/H] to standard $\alpha$-element trends may not be justified. Further, in the case of Y03, whose technique measured Ca II K EW, our analysis shows that Ca and Fe absorption in this region are highly degenerate, implying large uncertainties for the Y03 procedure. There does not appear to be a simple means of bringing about agreement between our result [Fe/H] $= -1$ and that of Y03, given the similar location of their targets at $(l,b) = (198^\circ,-27^\circ)$, $d_\odot = 13$ kpc and our field SOUTH at $(l,b) = (203^\circ,-24^\circ)$, $d_\odot = 12$ kpc. To whatever extent the present results disagree with those of C03 and Y03, our results should take precedence, as we have measured [Fe/H] directly, analyzing spectra with depth of exposure $\sim 7\times$ that of Y03 and S/N comparable to that of C03. Our sample size also eclipses that of C03 by a factor $>10\times$ and that of Y03 by a factor $\sim 1.5\times$.

Assuming the Monoceros progenitor contained stellar populations of varying age, we can still reconcile our result with that of the C03 M-giant sample, [Fe/H] $= -0.4 \pm 0.3$. M-giants preferentially trace younger, higher metallicity populations than MSTO stars. Carlin et al. (2012) have noted that this bias reconciles their MSTO Sgr stream [Fe/H] $= -1.15$ with literature M-giant values of [Fe/H] $\sim -0.6$. The Monoceros case appears directly analogous given our conclusion that Monoceros has MSTO [Fe/H] $= -1.0$. This reasoning can also bring about agreement between our [Fe/H] $= -1$ and the median [Fe/H] $= -0.71$ of the 21 kinematically selected M-giants studied by Chou et al. (2010b).

Since we have measured [Fe/H] directly from the Fe absorption lines of MSTO stars (a population with relatively little metallicity bias) and with S/N and sample size comparable to or better than previous spectroscopic efforts, we recommend adoption of our value [Fe/H] $= -1.0 \pm 0.1$ as the metallicity of the Monoceros stream.

### 6.2. The Metal Weak Thick Disk

Carollo et al. (2010) have speculated that the MWTD and Monoceros may share a common origin. This notion is based in part on the coincidence between the preliminary Wilhelm et al. (2005) estimate of Monoceros' metallicity, [Fe/H] $= -1.37$, and their inferred $\langle[\mathrm{Fe/H}]\rangle_{\mathrm{MWTD}} = -1.3$. Our measurements argue against this MWTD–Monoceros connection, as we find a $\sim$0.3 dex offset in [Fe/H] between these populations. All of our systematics are characteristically $\sim$0.05–0.10 dex, and, crudely speaking, we rule out a median [Fe/H] $= -1.3$ at the 2–3$\sigma_{\mathrm{syst}}$ level. Decreasing our median metallicity to $[\mathrm{Fe/H}]_{\mathrm{spec}} = -1.3$ would require, for example, an unreasonably large temperature scale miscalibration of $\sim$330 K.

### 6.3. The Monoceros Progenitor

Much controversy and speculation has surrounded the origin of the Monoceros structure since its discovery. To characterize the stream's nature, Y03 used star counts to estimate the total stellar mass of Monoceros at $\sim 2 \times 10^7\ M_\odot$–$5 \times 10^8\ M_\odot$, a range consistent with the content of a relatively luminous dwarf galaxy. Peñarrubia et al. (2005) specifically simulated the case of a dSph progenitor, fitting observations well with an initial progenitor of total mass 3–9 $\times\ 10^8\ M_\odot$. Still, detractors (e.g., Momany et al. 2006) argue that there is no need for an extragalactic origin of Monoceros. How can our observations further constrain the nature of the Monoceros progenitor?

The trends of $\langle[\mathrm{Fe/H}]\rangle$ and its dispersion, $\sigma_{[\mathrm{Fe/H}]}$, with dwarf galaxy luminosity have been studied by Norris et al. (2010), and are reproduced in Figure 8. Dwarf galaxy $\langle[\mathrm{Fe/H}]\rangle$ increases monotonically with luminosity; by fitting a linear trend in $\langle[\mathrm{Fe/H}]\rangle$ versus $M_V$ for $-2.1 < \langle[\mathrm{Fe/H}]\rangle < -0.9$, we can translate our MDF measurement $\langle[\mathrm{Fe/H}]\rangle \approx -1.0 \pm 0.1$ into a constraint on the Monoceros progenitor, $-13.2 \leqslant M_V \leqslant -12.3$, assuming the progenitor was a dwarf galaxy (see the dashed line and blue rectangle in Figure 8). Using a typical stellar mass-to-light ratio for dwarf galaxies $(M/L_V)_* \approx 3$ (Chilingarian et al. 2011), $\langle[\mathrm{Fe/H}]\rangle = -1$ implies $3.3 \times 10^7\ M_\odot$ of stellar mass in the Monoceros progenitor. Provided the fraction of the Monoceros progenitor which has been stripped is similar to that of Sgr (>2/3; Law & Majewski 2010), we conclude that our estimate of the stellar mass in the Monoceros stream based on chemistry and the assumption of a dwarf galaxy origin is consistent with the independent Y03 estimate from observed star counts. Having constrained the progenitor luminosity, we can also place Monoceros on the Figure 8 plot of $M_V$ versus $\sigma_{[\mathrm{Fe/H}]}$, finding very good qualitative agreement between Monoceros (blue rectangle) and other bright, low metallicity dispersion dwarf galaxies.

Instead of deriving $M_V$ from $\langle[\mathrm{Fe/H}]\rangle$, we can check whether a dSph progenitor with best-fitting mass determined by Peñarrubia et al. (2005) conforms the Norris et al. (2010) MDF trends. Taking the Monoceros stream to have the same total mass-to-light ratio as the Sgr core ($M_V = -13.3$, $M_{\mathrm{tot}} = 2.5 \times 10^8\ M_\odot$; Majewski et al. 2003; Law & Majewski 2010), the Peñarrubia et al. (2005) mass range translates to $-14.7 < M_V < -13.5$. We have combined this constraint with our measured MDF to plot the Peñarrubia et al. (2005) Monoceros progenitor (red rectangles) in Figure 8. In both cases, $M_V$ versus $\langle[\mathrm{Fe/H}]\rangle$ and $M_V$ versus $\sigma_{[\mathrm{Fe/H}]}$, Monoceros shows qualitative agreement with the dwarf galaxy trend.

Thus, we conclude that our abundance study supports a dwarf galaxy origin of Monoceros, in that (1) The MDF median and dispersion both conform to the expectations for an appropriately luminous dwarf galaxy progenitor and (2) we have detected [Ca/Fe] deficiencies typical of dwarf galaxy stellar populations in two of three fields observed.

### 6.4. Future Extensions

In the future, similar observations/analysis could be applied to Monoceros fields that more optimally search for $l$ and $b$ abundance gradients in the stream. For example, fixing $l$ and observing two $|Z|$ values symmetrically above/below the Galactic midplane would better isolate Monoceros abundance trends with $b$. Detecting or ruling out a gradient toward the midplane in this way would significantly constrain models which claim the stream to be a disk "warp" or "flare" (e.g., Momany et al. 2006). Observing an extended range of $l$ values at fixed $b$ would better constrain a metallicity gradient along the stream. For example, Sgr exhibits such a gradient, but only at the level $\sim 2.4 \times 10^{-3}$ dex per degree along the debris trail (Keller et al. 2010). To probe a gradient at this level with spectroscopy comparable to that reported here, observations would need to span $\sim 100^\circ$ in $l$, a factor of four increase relative to our current analysis, $178^\circ \leqslant l \leqslant 203^\circ$.

We warmly thank Nelson Caldwell for his advice on MMT observations, Hectospec details, and queue scheduling, as well as Evan Kirby and John Norris for fruitful discussions. We furthermore thank the queue observers and the SAO Telescope Data Center for reducing the data. This research made extensive use of the Vienna Atomic Line Database (VALD). A.M.M. is supported by a National Defense Science & Engineering Graduate fellowship. A.F. is supported by a Clay Fellowship administered by the Smithsonian Astrophysical Observatory. M.J. acknowledges support by NASA through Hubble Fellowship grant No. HF-51255.01-A awarded by the Space Telescope Science Institute, which is operated by the Association of Universities for Research in Astronomy, Inc., for NASA, under the contract NAS 5-26555.

*Facility:* MMT(Hectospec)

## REFERENCES

Asplund, M., Grevesse, N., Sauval, A. J., & Scott, P. 2009, ARA&A, 47, 481
Bensby, T., Zenn, A. R., Oey, M. S., & Feltzing, S. 2007, ApJ, 663, L13
Bond, N. A., Ivezić, Ž., Sesar, B., et al. 2010, ApJ, 716, 1
Briley, M. M., & Cohen, J. G. 2001, AJ, 122, 242
Carlin, J. L., Majewski, S. R., Casetti-Dinescu, D. I., et al. 2012, ApJ, 744, 25
Carollo, D., Beers, T. C., Chiba, M., et al. 2010, ApJ, 712, 692
Carretta, E., Bragaglia, A., Gratton, R., D'Orazi, V., & Lucatello, S. 2009, A&A, 508, 695
Chilingarian, I. V., Mieske, S., Hilker, M., & Infante, L. 2011, MNRAS, 412, 1627
Chou, M.-Y., Cunha, K., Majewski, S. R., et al. 2010a, ApJ, 708, 1290
Chou, M.-Y., Majewski, S. R., Cunha, K., et al. 2010b, ApJ, 720, L5
Cohen, J. G., & Meléndez, J. 2005, AJ, 129, 303
Conn, B. C., Lane, R. R., Lewis, G. F., et al. 2007, MNRAS, 376, 939
Crane, J. D., Majewski, S. R., Rocha-Pinto, H. J., et al. 2003, ApJ, 594, L119 (C03)
Fulbright, J. P. 2000, AJ, 120, 1841
Gratton, R. G., Carretta, E., Claudi, R., Lucatello, S., & Barbieri, M. 2003, A&A, 404, 187

Harris, W. E. 1996, AJ, 112, 1487
Ivezić, Ž., Sesar, B., Jurić, M., et al. 2008, ApJ, 684, 287 (I08)
Jurić, M., Ivezić, Ž., Brooks, A., et al. 2008, ApJ, 673, 864
Keller, S. C., Yong, D., & Da Costa, G. S. 2010, ApJ, 720, 940
Kurucz, R. L. 1993, VizieR Online Data Catalog, 6039, 0
Law, D. R., & Majewski, S. R. 2010, ApJ, 714, 229
Lee, Y. S., Beers, T. C., Sivarani, T., et al. 2008, AJ, 136, 2022
Majewski, S. R., Skrutskie, M. F., Weinberg, M. D., & Ostheimer, J. C. 2003, ApJ, 599, 1082
Marigo, P., Girardi, L., Bressan, A., et al. 2008, A&A, 482, 883
Martin, N. F., Ibata, R. A., Bellazzini, M., et al. 2004, MNRAS, 348, 12
Mink, D. J., Wyatt, W. F., Caldwell, N., et al. 2007, in ASP Conf. Ser. 376, Astronomical Data Analysis Software and Systems XVI, ed. R. A. Shaw, F. Hill, & D. J. Bell (San Francisco, CA: ASP), 249
Momany, Y., Zaggia, S., Gilmore, G., et al. 2006, A&A, 451, 515
Munn, J. A., Monet, D. G., Levine, S. E., et al. 2004, AJ, 127, 3034
Newberg, H. J., Yanny, B., Rockosi, C., et al. 2002, ApJ, 569, 245
Norris, J. E., Wyse, R. F. G., Gilmore, G., et al. 2010, ApJ, 723, 1632
Peñarrubia, J., Martínez-Delgado, D., Rix, H. W., et al. 2005, ApJ, 626, 128
Robin, A. C., Reylé, C., Derrière, S., & Picaud, S. 2003, A&A, 409, 523
Schlafly, E. F., & Finkbeiner, D. P. 2011, ApJ, 737, 103
Schlegel, D. J., Finkbeiner, D. P., & Davis, M. 1998, ApJ, 500, 525
Sesar, B., Jurić, M., & Ivezić, Ž. 2011, ApJ, 731, 4
Sneden, C. A. 1973, PhD thesis, Univ. Texas at Austin
Sobeck, J. S., Kraft, R. P., Sneden, C., et al. 2011, AJ, 141, 175
Wilhelm, R., Beers, T. C., Allende Prieto, C., Newberg, H. J., & Yanny, B. 2005, in ASP Conf. Ser. 336, Cosmic Abundances as Records of Stellar Evolution and Nucleosynthesis, ed. T. G. Barnes III & F. N. Bash (San Francisco, CA: ASP), 371
Yanny, B., Newberg, H. J., Grebel, E. K., et al. 2003, ApJ, 588, 824 (Y03)
Younger, J. D., Besla, G., Cox, T. J., et al. 2008, ApJ, 676, L21